J. Fluid Mech. (2002), *vol.* 455, *pp.* 149–174.
DOI: 10.1017/S0022112001007339 Printed in the United Kingdom

A computational model of the collective fluid dynamics of motile micro-organisms

By MATTHEW M. HOPKINS[1] AND LISA J. FAUCI[2]

[1]Plasma, Aerosol, and Noncontinuum Processes, Sandia National Laboratories, Albuquerque, NM, USA

[2]Department of Mathematics, Tulane University, New Orleans, LA 70118, USA

(Received 2 April 2001 and in revised form 21 September 2001)

A mathematical model and numerical method for studying the collective dynamics of geotactic, gyrotactic and chemotactic micro-organisms immersed in a viscous fluid is presented. The Navier–Stokes equations of fluid dynamics are solved in the presence of a discrete collection of micro-organisms. These microbes act as point sources of gravitational force in the fluid equations, and thus affect the fluid flow. Physical factors, e.g. vorticity and gravity, as well as sensory factors affect swimming speed and direction. In the case of chemotactic microbes, the swimming orientation is a function of a molecular field. In the model considered here, the molecules are a nutrient whose consumption results in an upward gradient of concentration that drives its downward diffusion. The resultant upward chemotactically induced accumulation of cells results in (Rayleigh–Taylor) instability and eventually in steady or chaotic convection that transports molecules and affects the translocation of organisms. Computational results that examine the long-time behaviour of the full nonlinear system are presented.

The actual dynamical system consisting of fluid and suspended swimming organisms is obviously three-dimensional, as are the basic modelling equations. While the computations presented in this paper are two-dimensional, they provide results that match remarkably well the spatial patterns and long-time temporal dynamics of actual experiments; various physically applicable assumptions yield steady states, chaotic states, and bottom-standing plumes. The simplified representation of microbes as point particles allows the variation of input parameters and modelling details, while performing calculations with very large numbers of particles ($\approx 10^4$–10^5), enough so that realistic cell concentrations and macroscopic fluid effects can be modelled with one particle representing one microbe, rather than some collection of microbes. It is demonstrated that this modelling framework can be used to test hypotheses concerning the coupled effects of microbial behaviour, fluid dynamics and molecular mixing. Thus, not only are insights provided into the differing dynamics concerning purely geotactic and gyrotactic microbes, the dynamics of competing strategies for chemotaxis, but it is demonstrated that relatively economical explorations in two dimensions can deliver striking insights and distinguish among hypotheses.

1. Introduction

The swimming trajectory of an individual motile micro-organism is determined by the action of its flagella and the advection by the bulk fluid flow. The orientation of its swimming velocity vector relative to the embedding fluid can be affected by a variety of external factors including nutrient concentration, gravity, and the vorticity

and rate of strain of the fluid. For example, consider cells such as the algal cell *Chlamydomonas nivalis*, which propel themselves by performing a 'breast-stroke' with their two anterior flagella. These 'bottom heavy' cells tend to swim upwards due to the anisotropic mass distribution of organelles within their cell body. An upwards swimming tendency is termed negative *geotaxis* or negative *gravitaxis* (see Kessler 1986). The orientation of a motile micro-organism is also affected by gradients in the local fluid velocity. Its swimming is vorticity-sensitive in that a local rotation of the flow tends to incline the swimming axis. In the present context, the angle between the axis of the cell and the vertical direction depends upon the rotational viscous drag and the distance between the centre of volume and the centre of mass. Swimming oriented by this mechanism is termed *gyrotaxis* (see Kessler 1986*b*).

The tendency of cells to swim up or down a chemical concentration gradient is called *chemotaxis*. Bacterial cells such as *Bacillus subtilis* and *Escherichia coli* swim by rotating flagella driven by reversible motors embedded in the cell wall. The motion of these cells can be described by run intervals during which the cells swim approximately in a straight line, interspersed with tumbles during which the organism undergoes random reorientation. Chemotactic bacteria sense temporal changes in nutrient concentration. It is generally thought that, if the sensed concentration level changes, the bacteria respond by appropriately changing their tumbling probability. Thus, run times are longer when bacteria swim up a chemoattractant gradient. Berg (1983) summarized the operation of this most prevalent mode of bacterial chemotaxis.

Although individual cells in a suspension are independently guided by these external cues, their interactions are mediated through the fluid. Bioconvection, the collective behaviour of a concentrated population of cells, may give rise to sustained, relatively steady or time-varying spatial patterns. For example, bioconvection occurs when the upward-swimming cells cause an unstable density stratification large enough to trigger a Rayleigh–Taylor instability in the form of descending plumes. In such a plume, the fluid velocity overcomes the upward swimming velocity of individual cells. Figure 1 shows a series of snapshots of a suspension of the aerobic bacteria *B. subtilis*. Initially the suspension is uniform. Upswimming occurs because of the source of oxygen at the upper surface. Note that the initial instabilities at the surface eventually cause downwelling plumes. These plumes advect oxygen throughout the region (see Kessler *et al.* 1995).

Bioconvection has been studied experimentally (e.g. Plesset & Winet 1974; Kessler 1989), analytically (e.g. Levandowsky *et al.* 1975; Pedley, Hill & Kessler 1988; Hill, Pedley & Kessler 1989; Pedley & Kessler 1990, 1992; Hill 1997, pp. 339–351; Metcalfe & Pedley 1998) and numerically (e.g. Childress & Peyret 1976; Harashima, Watanabe & Fujishiro 1988; Ghorai & Hill 1999, 2000*a*, *b*). Much progress has been made in the development of continuum models of this dynamical system, where the micro-organisms are represented by a continuous cell-density distribution. The coupled partial differential equations that describe the fluid–micro-organism suspension are amenable to mathematical analysis including linear stability analysis.

In this paper we present a mathematical model and numerical method that solves the coupled fluid–micro-organism–nutrient system. In contrast to continuum models, we represent the micro-organisms as a suspension of discrete particles within the fluid domain. In the spirit of the work of Childress & Peyret (1976), the microbes act as point sources of mass in the continuous Navier–Stokes equations, and thus affect the fluid flow. In addition, the fluid flow affects the swimming orientation of microbes in a number of ways. Each microbe is advected by the fluid. In the case of gyrotactic microbes, the swimming orientation is a function of the gradients of the

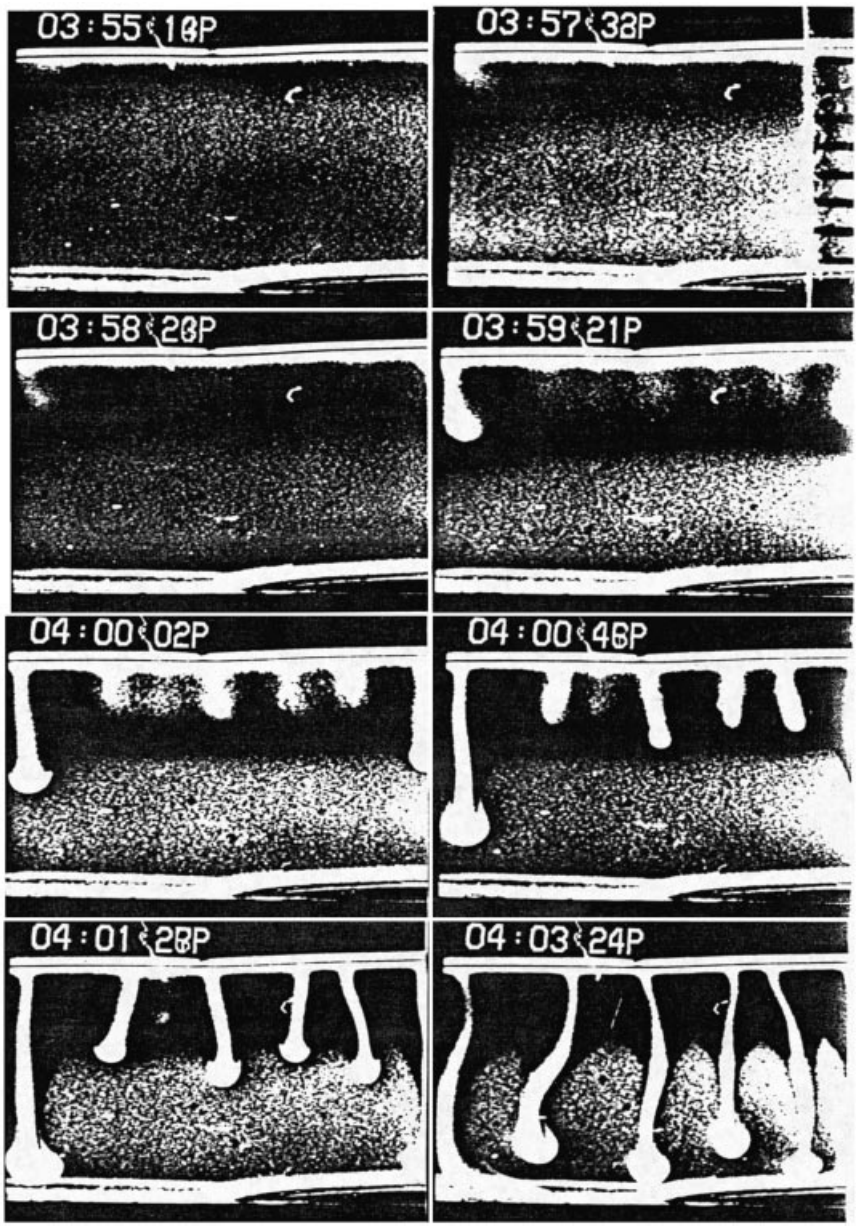

FIGURE 1. A series of snapshots of a suspension of the aerobic bacteria *B. subtilis*. Initially the suspension is uniform. Upswimming occurs because of the source of oxygen at the upper surface. Note that the initial instabilities at the surface eventually cause downwelling plumes. (Courtesy of J. O. Kessler.)

fluid velocity field. In the case of chemotactic microbes, the swimming orientation is a function of the nutrient field, which diffuses in and is advected by the fluid that convects due to non-uniform accumulation of organisms. Swimming directions and swimming speeds of micro-organisms are influenced by both chemotaxis and the velocity field of the fluid. In addition, the nutrient may be consumed by the microbes,

whose swimming speed may also be a function of nutrient concentration (see Kessler, Burnett & Remick 2000).

The discrete representation of microbes by individual particles rather than by a continuous cell-density concentration facilitates the direct evaluation of cell orientation in response to environmental cues, as well as the superposition of stochastic distributions that represent cell-to-cell variability in speed and orientation. Although we choose a discrete representation of microbes, we do not seek to capture in detail the geometry, flagellar action and local dynamics of the organisms as do the microscale models presented in Dillon, Fauci & Gaver (1995), Jones, LeBaron & Pedley (1994) and Ramia, Tullock & Phan-Thien (1993). However, our simplified representation of microbes as point particles allows us to perform calculations with very large numbers of particles – enough so that realistic cell concentrations and macroscopic fluid effects can be modelled with one particle representing one microbe, rather than some collection of microbes.

In the following sections we will present the mathematical model and numerical method that together provide a unified approach for the investigation of the macroscopic flows that result from the collective behaviour of organisms denser than the suspending fluid. The collective behaviour consists of geotaxis, gyrotaxis, and chemotaxis, all of which depend upon the flow field characteristics. Thus the system is nonlinear, not only in the governing equations, but also in their interdependence. Computational results that examine the long-time behaviour of the full nonlinear system will be presented.

2. Mathematical model

2.1. *Fluid dynamics*

We assume that the fluid is homogeneous and incompressible, and the volume fraction of the micro-organisms is so small as to have a negligible effect on the inertia and the viscosity μ of the fluid–microbe suspension. Indeed, we make the Boussinesq approximation and assume that the average density of the fluid–microbe suspension is that of the fluid ($\bar{\rho} = \rho_{\text{fluid}}$). The density of an individual microbe $\rho_m = \rho_{\text{fluid}} + \Delta\rho$ is assumed to be slightly greater than the density of the fluid. Even though $\Delta\rho \ll \rho_{\text{fluid}}$, the force due to gravity on each microbe must be included in the momentum equation below.

We consider a rectangular region of fluid in which a collection of N discrete micro-organisms located at $\boldsymbol{x}_k, k = 1, 2, \ldots, N$ is immersed. These microbes have density ρ_m, volume v_m, and their swimming speeds and orientations are denoted by $s_k(t)$ and $\boldsymbol{p}_k(t)$ respectively.

We adopt a continuum description of the fluid, and assume that the flow is governed by the incompressible Navier–Stokes equations. In our studies of chemotactic organisms, we also track a chemical with concentration $c(\boldsymbol{x}, t)$ that is advected by and diffuses in the fluid, and is consumed by the microbes. Our coupled fluid–microbe–chemical system is, therefore, governed by the following equations:

$$\bar{\rho}\left(\frac{\partial \boldsymbol{u}}{\partial t} + \boldsymbol{u}\cdot\nabla\boldsymbol{u}\right) = -\nabla p + \mu\nabla^2\boldsymbol{u} + \Delta\rho v_m \boldsymbol{g}\sum_{k=1}^{N}\delta(\boldsymbol{x}-\boldsymbol{x}_k), \tag{2.1}$$

$$\nabla\cdot\boldsymbol{u} = 0, \tag{2.2}$$

$$\frac{\partial c}{\partial t} + \boldsymbol{u} \cdot \nabla c = D\nabla^2 c - R(c) \sum_{k=1}^{N} \delta(\boldsymbol{x} - \boldsymbol{x}_k), \tag{2.3}$$

$$\frac{\mathrm{d}\boldsymbol{x}_k}{\mathrm{d}t} = \boldsymbol{u}(\boldsymbol{x}_k, t) + s_k \boldsymbol{p}_k, \quad k = 1, 2, \ldots, N. \tag{2.4}$$

Here $\boldsymbol{u} = \boldsymbol{u}(\boldsymbol{x}, t)$ is the fluid velocity, $p = p(\boldsymbol{x}, t)$ is the pressure and μ is the fluid viscosity. Note that (2.1) contains a source term that accounts for the added mass due to each of the microbes, labelled by the index k. Here, δ is the Dirac delta function, and $\boldsymbol{g}$ is the acceleration due to gravity, pointing downward. In the evolution equation (2.3) for the chemical, D is the diffusivity, and $R(c)$ is the consumption rate which depends upon the local concentration and may be chosen to reflect particular uptake kinetics. In particular, we choose a form that is motivated by Hillesdon, Pedley & Kessler (1995) (see equation (5.3) in § 5.1). The consumption is only non-zero at the sites of the microbes, which act as point sinks.

Unlike the traditional models of bioconvection and chemotaxis, we do not assume a continuous distribution of microbes $n(\boldsymbol{x}, t)$. The conservation of cell concentration n, where $\boldsymbol{J}$ is the cell flux including swimming and advection,

$$\frac{\partial n}{\partial t} = -\nabla \cdot \boldsymbol{J}, \tag{2.5}$$

has been replaced by the discrete equation (2.4) above. The first term on the right-hand side of (2.4) represents the advection of the micro-organism by the bulk fluid flow, and the second term represents the micro-organism's motion relative to the fluid.

We designate the time-dependent swimming direction of the kth micro-organism by an orientation unit vector, $\boldsymbol{p}_k$, or a single orientation angle, $\theta_k(t)$, so that

$$\boldsymbol{p}_k = (\sin\theta_k, -\cos\theta_k), \tag{2.6}$$

with $0 \leqslant \theta_k < 2\pi$.

The functions s_k and θ_k will depend upon the external cues and intrinsic variability that influence the micro-organism's motion. For instance, the swimming speed s_k may depend upon the concentration c at the cell location. The evolution of the orientation angle will be governed by a torque balance equation. The torques that model geotaxis, gyrotaxis and chemotaxis are described below.

2.2. *Geotaxis*

The tendency of an organism to swim up (or down) in the gravitational field of the Earth is called *geotaxis* or *gravitaxis*. In some algae, geotaxis occurs because the centre of mass is offset from the centre of buoyancy. This offset results in an up-righting gravitational torque. In two dimensions, this scalar torque is

$$\tau_{\mathrm{geo}} = m_m g h \sin\theta_k, \tag{2.7}$$

where m_m is the mass of the micro-organism, g is the gravitational constant, and h is the (positive) distance that the centre of mass is offset from the centre of buoyancy. We assume that the centre of mass is offset in a direction directly opposite the swimming direction, as in *C. nivalis* (see Kessler 1986*a*). The $\theta_k = 0$ configuration is unstable, whereas the $\theta_k = \pi$ configuration is stable, and represents the situation where the micro-organism is oriented straight up ($\boldsymbol{p}_k = (0, 1)$).

2.3. *Gyrotaxis*

Gyrotaxis results from a combination of a geotactic torque and a torque due to the local vorticity of the fluid. In the presence of a non-zero vorticity, the micro-organism will experience a torque causing it to rotate. For spheres, the magnitude of this vorticity-induced torque is given by

$$\tau_{\text{vort}} = 4\pi\mu r_m^3(\nabla \times \boldsymbol{u}) \cdot (0, 0, 1), \tag{2.8}$$

where r_m the radius of the sphere. This result, due to Faxén, and its ramifications are described by Happel & Brenner (1987). Situations where the flow is complex and the swimming organisms nonspherical were discussed by Pedley & Kessler (1987).

When this vorticity-induced torque is coupled with the torque given by geotaxis, two different effects can occur. The torque due to vorticity may be so large that the geo-orientation response is overcome, and the micro-organisms rotate 'end-over-end' at a non-uniform rate. At smaller turning moments, the torques balance at some intermediate orientation. Pedley & Kessler (1992) present a more detailed discussion of these two effects, and the transition from one to another.

We are particularly interested in the situation when a gyrotactic micro-organism is near a plume. Then, the fluid nearby has a non-zero vorticity. To the right of a downward plume, the vorticity is positive, and to the left the vorticity is negative. This affects the micro-organism's orientation so that it rotates towards the downwelling region of the fluid, or, alternatively, it rotates away from the upwelling region. Because the micro-organisms swim into the downward plumes, we expect gyrotactic micro-organisms to reinforce downwelling regions more locally and hence faster than purely geotactic ones.

2.4. *Chemotaxis*

Because the evolution of an entrained chemical can be tracked at individual cell sites as well as in the entire fluid region, we can implement a variety of models of chemotaxis. Herein, we consider only *chemoattractants* where the micro-organisms favour levels of higher chemical concentrations.

In the first model, we assume that the micro-organism can directly detect spatial gradients in $c(\boldsymbol{x}, t)$, and can identify a preferred orientation, θ_g, pointing in the direction of most-steeply increasing chemical concentration. We further assume that there is some cutoff gradient magnitude, below which the cell cannot detect the preferred direction (see Hillesdon *et al.* 1995). We model as an 'effective torque' the behavioural reaction to the sensory input provided by the ∇c. This effective torque is given by

$$\tau_{\text{chemo}} = -(\theta_k - \theta_g)H(|\nabla c| - \epsilon). \tag{2.9}$$

Here H is the Heaviside step function and ϵ is the prescribed cutoff. This effective torque will be multiplied by a weight parameter representing the relative strength of this torque compared to the torques due to geotaxis and gyrotaxis in solving for the orientation of the kth microbe.

We may also implement chemotactic strategies that rely upon the time history of the chemical along cell trajectories as in a run-and-tumble model of bacterial chemotaxis. The micro-organism retains a short history of its local chemical concentration. The probability of a reorientation (tumble) is greater if the cell's history indicates a drop in the chemical concentration. This causes the micro-organisms to move, on average, into regions of higher chemical concentration. We use the model described in Dillon *et al.* (1995) to determine the probability of a reorientation.

The velocity of a micro-organism may also be affected by its local chemical concentration (see Pedley & Kessler 1992; Dillon *et al.* 1995; Hillesdon *et al.* 1995; Kessler *et al.* 1995; Hill 1997, pp. 339–351). For instance, if the chemical concentration falls below a certain threshold, the micro-organism may cease to be motile.

More detailed discussion of the particular choices of chemotaxis strategies, motility dependence on chemical concentrations, and microbial consumption of chemical will be presented below.

2.5. *Evolution of orientation* θ_k

The orientation vector $\boldsymbol{p}_k$ is determined by an orientation angle θ_k that is governed by the torque balance equation,

$$I\frac{\mathrm{d}^2\theta_k}{\mathrm{d}t^2} = \alpha_{\mathrm{geo}}\tau_{\mathrm{geo}} + \alpha_{\mathrm{vort}}\tau_{\mathrm{vort}} + \alpha_{\mathrm{chemo}}\tau_{\mathrm{chemo}} - \alpha_{\mathrm{damp}}\beta\frac{\mathrm{d}\theta_k}{\mathrm{d}t}, \tag{2.10}$$

where the τ are defined in the previous sections, I is the moment of inertia, $\beta = 8\pi\mu r_m^3$ is the coefficient for viscous damping. The coefficients α determine the weight of the particular torque. If the particles represent spheres, the coefficients α_{vort} and α_{damp} are equal. This need not be the case when the point particles represent various organisms which could be active, passive and of arbitrary shape. Our model is specifically constructed to quantitatively examine the effects of different orientation mechanisms. This is achieved by allowing independent variation of the weight coefficients.

In order to account for cell-to-cell variability within the population, a random component chosen from a normal distribution is applied to θ_k. It should be noted that a large vorticity field (or, equivalently, a large α_{vort}) may cause a cell to flip 'end-over-end'. This is discussed in detail in Pedley & Kessler (1987).

The exception to the above formulation is the run-and-tumble model of chemotaxis, which is not formulated in terms of an effective torque. An example of a run-and-tumble simulation is presented in figure 16.

3. Numerical method

3.1. *Fluid and chemical solver*

Although the mathematical model described in the previous section is three-dimensional, we will present results of the two-dimensional analogue of this model. To adjust for two-dimensionality in computing the velocity source term, we replace the micro-organism volume v_m with a micro-organism area $a_m = \pi r_m^2$ computed using the radius of the three-dimensional sphere with volume v_m,

$$r_m = \left(\frac{3v_m}{4\pi}\right)^{1/3}. \tag{3.1}$$

Although we use a_m in the velocity source term, all of the cell torque computations are based on the three-dimensional geometry. This is consistent with the analytic models of Kessler (1986*a*), Pedley *et al.* (1988), Hill *et al.* (1989) and Pedley & Kessler (1990).

The numerical solution of the Navier–Stokes equation is based on the SIMPLE (Semi-IMplicit Pressure Linked Equations) finite volume method described in Patankar (1980) and uses the SIMPLEC modification described in van Doormaal & Raithby (1984). This method is also used to solve the chemical transport equation. The SIMPLE method is based on a balance of fluxes. A two-dimensional rectangular domain is decomposed into an array of rectangular control volumes. The flux over each of

the four volume interfaces is calculated by using the analytic solution of a one-dimensional transport equation. These fluxes are set equal to the average source term over the same volume. This yields a system of equations for each of the unknowns. In order to satisfy incompressibility, an iterative pressure-correction scheme is also implemented. For details, see Patankar (1980) and van Doormaal & Raithby (1984).

The fluid domain is covered with a uniform rectangular grid with grid spacing Δx and Δy in the horizontal and vertical directions, respectively. The discrete microbes are represented as a list of positions (x_k, y_k), with associated orientation angles θ_k, where $k = 1, \ldots, N$. In interpreting our cell concentrations, we assume that M cells per unit area in our two-dimensional domain correspond to $M^{3/2}$ cells per unit volume in a three-dimensional domain. In the simulations shown in this paper, we choose $N \approx 10^4$–10^5, which corresponds to a three-dimensional cell concentration of 10^6–3×10^7 cells cm^{-3}.

The microbe points are free to move throughout the fluid domain, and will affect the fluid directly through the source term in (2.1). Since the fluid variables are defined on the Eulerian grid, we must distribute the added mass due to the microbes at nearby grid locations. This is done by means of a discrete approximation to the Dirac delta function,

$$\boldsymbol{F} \approx (\bar{\rho} - \rho_m) a_m \boldsymbol{g} \sum \hat{\delta}(x_k - x, y_k - y), \tag{3.2}$$

where the Dirac delta function approximation is given by

$$\hat{\delta}(x, y) = \begin{cases} \dfrac{1}{\Delta x \Delta y} \left(1 - \dfrac{|x|}{\Delta x}\right) \left(1 - \dfrac{|y|}{\Delta y}\right) & \text{if } |x| < \Delta x \text{ and } |y| < \Delta y \\ 0 & \text{otherwise.} \end{cases} \tag{3.3}$$

Using this approximation, we allocate the mass of each microbe to the i, j location on the grid with

$$\boldsymbol{F}_{i,j} = (\bar{\rho} - \rho_m) a_m \boldsymbol{g} \sum \hat{\delta}(x_k - x_i, y_k - y_j). \tag{3.4}$$

Here (x_i, y_j) indicates the spatial positions of the i, j grid point. Note that each microbe contributes weight to at most four of the grid points. In addition, this discrete Delta function is used to account for the microbial consumption of the chemical in (2.3).

Conversely, grid values of velocity and chemical concentration must be interpolated to the Lagrangian microbes to update their positions in (2.4), as well as to evaluate their swimming speeds, gyrotactic torques, and chemotactic responses. This is done by simple bilinear interpolation.

3.2. *Microorganism motility equations*

In order to solve (2.10) numerically, we note that the coefficient of inertia I is sufficiently small so that the term $I \mathrm{d}^2\theta_k/\mathrm{d}t^2$ can be neglected. This reduces the ODE from second to first order. We performed computations that solved the full second order ODE to very high precision, and compared these solutions to those with the above assumption,

$$\frac{\mathrm{d}\theta_k}{\mathrm{d}t} = (\alpha_{\mathrm{damp}}\beta)^{-1}(\alpha_{\mathrm{geo}}\tau_{\mathrm{geo}} + \alpha_{\mathrm{vort}}\tau_{\mathrm{vort}} + \alpha_{\mathrm{chemo}}\tau_{\mathrm{chemo}}), \tag{3.5}$$

over typical run parameters (i.e. torque strengths, timesteps, initial distributions of θ_k) and we found the difference to be very small ($\approx 10^{-5}$ relative error).

We solve (3.5) using the forward Euler method, with a random component added

to represent cell-to-cell variability,

$$\theta_k^{n+1} = \theta_k^n + \Delta t \frac{\mathrm{d}\theta_k}{\mathrm{d}t} + N(\mu_\theta, \sigma_\theta \Delta t), \tag{3.6}$$

where $\mathrm{d}\theta_k/\mathrm{d}t$ is found by computing all of the relevant torque terms in (3.5) at the end of the nth timestep, and $N(a, b)$ is a random variable chosen from a normal distribution with mean a and standard deviation b. Since this random variable is being added to the direction angle, it is applied modulo 2π.

In the case of no dependence on an entrained chemical, the speed s_k of the micro-organism is easily calculated,

$$s_k = s_0 + N(\mu_s, \sigma_s \Delta t). \tag{3.7}$$

In practice, we choose $\mu_s = 0$ and $\sigma_s = 0.1 s_0\,\mathrm{s}^{-1}$, so the chances of the swimming speed becoming negative are negligible. In the case of a functional dependence upon available chemical, we have

$$s_k = f(c(\boldsymbol{x}_k, n\Delta t)) + N(\mu_s, \sigma_s \Delta t), \tag{3.8}$$

where $c(\boldsymbol{x}_k, n\Delta t)$ is evaluated at the microbe site by bilinear interpolation, and $f(c)$ is a prescribed function (see equation (5.2) in § 5.1).

The microbe locations are updated by

$$\boldsymbol{x}_k^{n+1} = \boldsymbol{x}_k^n + \Delta t(\boldsymbol{u}(\boldsymbol{x}_k) + s_k \boldsymbol{p}_k), \tag{3.9}$$

where $\boldsymbol{p}_k = (\sin\theta_k, -\cos\theta_k)$ is the unit vector associated with θ_k.

3.3. *Computational algorithm*

The state of the system at the end of timestep n is given by the fluid velocity field $\boldsymbol{u} = (u, v)$, chemical field c, microbial locations $\boldsymbol{x}_k$ and orientations θ_k. Our numerical method for advancing the full system from timestep n to timestep $n+1$ is as follows:

(*a*) evaluate the source terms on the grid in (2.1) and (2.3) using the discrete Delta function;

(*b*) use the solutions from the previous timestep as initial guesses to iterate the u, v, and p solutions to the Navier–Stokes equations until sufficiently converged (using the SIMPLE method);

(*c*) using the new u and v solutions, solve for c using the SIMPLE method, using appropriate boundary conditions;

(*d*) for each microbe, evaluate the torques:

(i) if geotaxis is activated, calculate $mgh\sin\theta_k$;

(ii) if gyrotaxis is activated, calculate torque by interpolating $\nabla \times \boldsymbol{u}$ to microbial locations;

(iii) if spatial gradient chemotaxis is activated, interpolate values of ∇c to microbial locations;

(iv) using the torque balance equation (3.5) find the new θ_k;

(v) find s_k by interpolating $c(\boldsymbol{x}_k, n\Delta t)$, if necessary;

(vi) apply random effects $N(\mu_s, \sigma_s \Delta t)$ and $N(\mu_\theta, \sigma_\theta \Delta t)$

alternatively, in the case of 'run-and-tumble' chemotaxis:

(i) save current local chemical concentration to chemical history;

(ii) reorient if necessary to get the new θ_k;

(iii) find s_k by interpolating $c(\boldsymbol{x}_k, n\Delta t)$, if necessary;

(iv) apply random effects $N(\mu_s, \sigma_s \Delta t)$

(*e*) update each micro-organism location using (3.9).

Description	Symbol	Value
Cell density	ρ_m	$1.05\,\mathrm{g\,cm^{-3}} = 1.05\rho$
Cell volume	v_m	$1.70 \times 10^{-11}\,\mathrm{cm^3}$
Base cell swimming speed	s_0	$75\,\mu\mathrm{m\,s^{-1}}$
Centre of gravity offset	h	$0.05 r_m$

TABLE 1. Physical cell characteristics for *Chlamydomonas nivalis* algal cell given in Kessler (1986*a*), and used in all of the geotaxis and gyrotaxis simulations presented in this section.

4. Numerical results: geotaxis and gyrotaxis

We consider the rectangular, horizontally periodic fluid domain, $\Omega_R = [0, l] \times [0, H]$, where H varies from 8 mm to 14 mm, and $l = 8$ cm. We choose stress-free boundary conditions for the fluid velocity at the upper surface $y = H$: $u_y = 0$ and $v = 0$. (Allowing tangential slip at the surface, rather than imposing zero flow at a rigid boundary, has the effect of accelerating the onset of downwelling instabilities. Otherwise, the qualitative dynamics are essentially the same as those presented below.) At the bottom of the rectangle $y = 0$, the fluid velocity is zero. The $N_x \times N_y$ numerical mesh is set so that $N_x = 120$ and $N_y = 12 + M$, where $M = 0$, 3, 6, and 9 for the 8, 10, 12, and 14 mm heights. This gives a fixed horizontal and vertical mesh spacing of $\Delta x = \Delta y = 0.6667$ mm.

To keep the cell concentration constant, we increased N_m with fluid domain height. We used $N_m = 100\,000$ cells at 14 mm as the reference cell concentration ($N_m = 57\,143$ at 8 mm). This gave a three-dimensional cell concentration of $\approx 8.44 \times 10^5\,\mathrm{cells\,cm^{-3}}$. (Recall that in interpreting our cell concentrations, we assume that M cells per unit area in our two-dimensional domain correspond to $M^{3/2}$ cells per unit volume in a three-dimensional domain.) The initial cell distribution was random and uniform ($x \in U[0, l], y \in U[0, H]$) for each run ($U[a, b]$ has the flat density function $1/(b - a)$ over the interval $[a, b]$, and 0 elsewhere). The solution is advanced for 1600 s, using a timestep $\Delta t = 0.2667$ s. The following calculations were performed on a single processor SGI IRIS workstation, and required CPU time on the order of 4–6 hours.

The fluid density was taken to be $\rho = 1\,\mathrm{g\,cm^{-3}}$, and the fluid viscosity was $\mu = 0.0175\,\mathrm{g\,cm^{-1}\,s^{-1}}$. The micro-organism parameters we used are defined in table 1 (taken from data for the *C. nivalis* algal cell in Kessler 1986*a*). Random components were chosen to be $\mu_\theta = 0$ rad, $\sigma_\theta = \pi/4\,\mathrm{rad\,s^{-1}}$, $\mu_s = 0\,\mu\mathrm{m\,s^{-1}}$, and $\sigma_s = 0.1 s_0\,\mathrm{s^{-1}}$.

Hill & Häder (1997) present statistical data on the swimming speeds and orientations of motile algal cells in suspensions. In particular, they measure the mean and the standard deviation of swimming speeds of an ensemble of both *Chlamydomonas nivalis* and *Peridinium gatunense* in a vertical plane. The mean swimming speeds reported for these cells are $\approx 40\,\mu\mathrm{m\,s^{-1}}$ and $\approx 75\,\mu\mathrm{m\,s^{-1}}$, respectively. In addition, the standard deviations are reported to be $\approx 30\,\mu\mathrm{m\,s^{-1}}$ and $\approx 10\,\mu\mathrm{m\,s^{-1}}$, respectively. Therefore, our computational microbes' swimming speed of $75\,\mu\mathrm{m\,s^{-1}}$ is consistent with measured data. However, the standard deviation used in the computations represents a more homogeneous population than those measured experimentally.

The geotaxis and gyrotaxis simulations at all heights initially progress in the same way. First, the cells in the initial distribution swim, on average, towards the surface. As the cell density at the surface grows, a series of alternating downwelling and upwelling regions form. After some time, the velocities in the downwelling regions overcome the swimming speeds of the cells, and the fluid/micro-organism plumes begin their

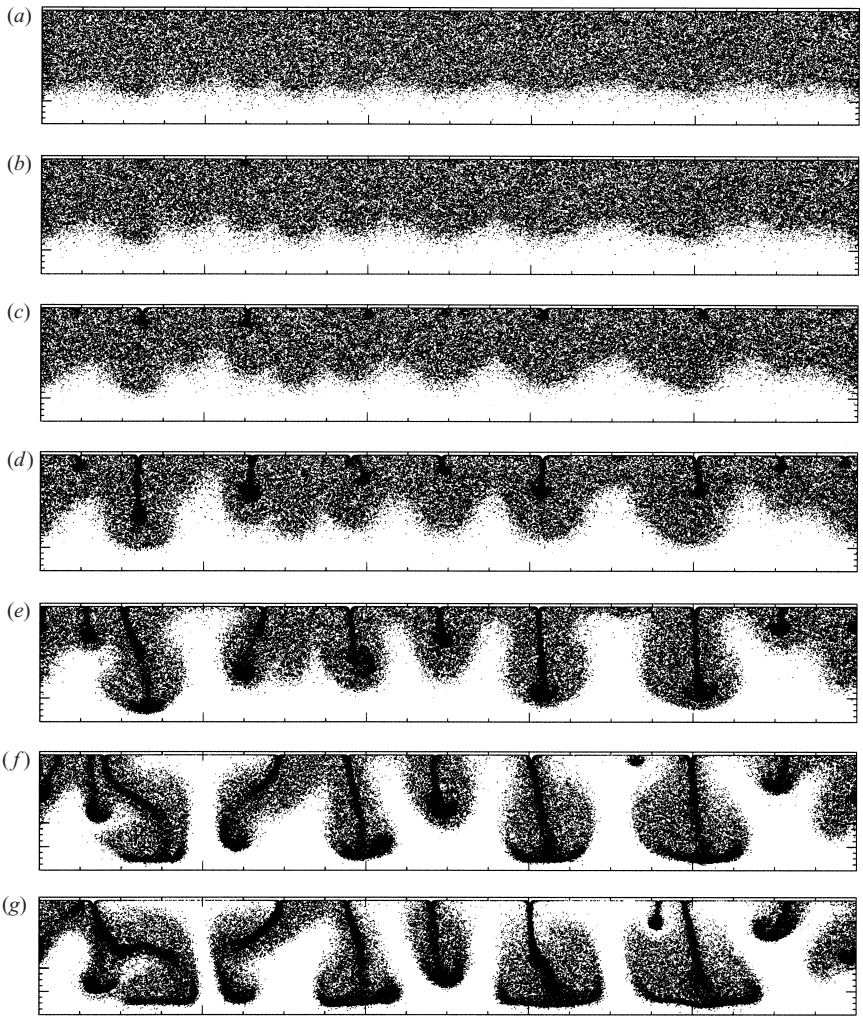

FIGURE 2. A sequence of snapshots capturing the initial overturning from a 12 mm geotactic run. Note that all of the approximately 85 700 particles representing the discrete microbes are depicted. Snapshots taken at times (*a*) 72 s, (*b*) 80 s, (*c*) 88 s, (*d*) 96 s, (*e*) 104 s, (*f*) 112 s, (*g*) 120 s.

descent. The maximum fluid velocities grow monotonically until the plumes descend. See figure 2(*a–g*) for an example of the initial overturning for geotactic cells. The plumes reach the bottom, and the initial 'catastrophic' overturning instability is over.

After the initial overturning occurs, the cells are still oriented to swim towards the surface (which they do in the regions between plumes). However, although they are oriented upwards in a plume, the fluid velocity overcomes their upwards swimming, and they are swept downwards. In a well-defined plume, the cells repeat a general movement pattern: they fall in the downwelling region, reach the bottom of the plume, move left or right into the plume's periphery, then swim and are advected by the fluid towards the surface, and then fall back into the downwelling region. Under some conditions the plume remains very steady, while in others it dissipates as soon as the initial collection of cells that caused it reaches the bottom. This essential difference is one of the plume characteristics we wish to measure.

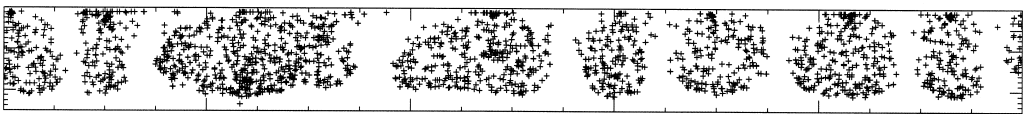

FIGURE 3. These plumes in a particular 8 mm height run were stable for approximately 700 s before the second one absorbed the first. While only 2000 particles representing the discrete microbes are shown, this calculation was performed with over 57 000 particles.

To measure the plume spacing at a single output time, we subdivide the domain into 512 vertical strips of equal width. We define f_i to be the number of cells in each vertical strip ($i = 1, \ldots, 512$). We define $f(x)$ to be the (unknown) function that the f_i approximate, so that $f((i-0.5)/512) \approx f_i$. We apply some smoothing to f_i by replacing it with a weighted average of f_i, f_{i-1} and f_{i+1}. We then take the discrete Fourier transform of f_i to obtain the Fourier coefficients a_n, b_n in the expansion

$$f(x) \approx \sum_n a_n \cos\left(\frac{n\pi x}{l}\right) + ib_n \sin\left(\frac{n\pi x}{l}\right), \tag{4.1}$$

and find the wavenumber, d, of the wave with maximum amplitude ($\sqrt{a_d^2 + b_d^2} \geqslant \sqrt{a_n^2 + b_n^2}$). We define $\gamma = l/d$ to be the wavelength of the wave of maximum amplitude. In the case of stable equal-width plumes, γ measures the spacing between the plume centres.

Because of the transient nature of the solution, we sample the solution at every 8 s for the last 800 s of the run (so that the solution has time to reach a pseudo-steady state, if there is one) to obtain a series of wavelengths, γ_i, and wavenumbers, d_i, for $i = 1, \ldots, 100$. We define $\bar{\gamma}$ and σ_γ to be the mean and standard deviation of the γ_i, and $\bar{d}$ and σ_d to be the mean and standard deviation of the d_i. We may interpret σ_d as a measure of the persistence or stability of the plumes. Unfortunately, there exist stable patterns of variable-width plumes. This causes a non-constant d_i and non-zero σ_d even though the plumes are very stable. For this reason, we shall report a visual number of plumes d_{vis} when the last output indicates a discernible plume formation (we use +0.5 for partial plumes). See figure 3 for an example of stable varying width plumes.

In a steady plume, cells tend to travel in a series of loops. We approximate the period of this loop by performing a discrete Fourier transform on the height of the cell over the last 800 s, to avoid the initial transients. This is done for 2000 sample cells. We take the average of this cycle time over the 2000 cells and report it as t_{cycle}. We also report the standard deviation of cycle time per cell for each of the 2000 sample cells over the last 800 s, σ_{cycle}. This is an indicator of the consistency of the time the cells require to cycle from top to bottom.

4.1. *Geotaxis results*

We first consider purely geotactic cells ($\alpha_{\text{geo}} = 1$, $\alpha_{\text{damp}} = 3.09$, and all other α values $= 0$). To account for the variability from one run to the next because of the randomness in micro-organism orientation and swimming speed, we performed five runs at each of the heights: 8, 10, 12 and 14 mm. We also performed five runs at 8 mm with a double width domain (16 cm) on a mesh of size $N_x = 162$, $N_y = 14$. The initial cell orientations were taken from the uniform distribution $\theta \in U[0, 2\pi)$. Table 2(a) reports the mean over all five runs for each of the fluid heights, and table 2(b) reports the median (to exclude possible outliers) for each of the fluid heights. A typical pseudo-steady state is presented in figure 4.

	H	avg.$\bar{\gamma}$	avg.$\bar{d}$	avg.σ_d	avg.d_{vis}	avg.t_{cycle}	avg.σ_{cycle}
(*a*)	8	1.18	7.25	0.92	6.70	147.3	31.0
	10	1.98	5.60	1.51	5.10	116.9	48.8
	12	2.03	4.63	1.95	4.30	181.2	61.1
	14	2.08	4.50	1.83	3.63	192.1	60.7
	8†	1.40	6.00	0.99	6.50	151.5	49.5
(*b*)	8	1.14	7.00	0.86	7.0	142.4	21.30
	10	1.30	6.45	1.67	5.5	164.5	46.55
	12	1.89	4.80	1.58	4.5	190.7	68.63
	14	2.02	4.63	1.66	3.5	183.2	59.62
	8†	1.30	6.69	0.87	6.8	149.0	47.02

TABLE 2. Average values (*a*) by *mean* and (*b*) by *median* of computed wavelength $\bar{\gamma}$, wavenumbers $\bar{d}$, standard deviation of wavenumbers σ_d, visual number of plumes d_{vis}, the cycle time of a particle through a plume t_{cycle}, and the standard deviation of this cycle time σ_{cycle}. These are shown for each height h. †Runs used a 16 cm width and values for d and d_{vis} have been halved in order to compare with the 8 cm width runs.

H	$\bar{\gamma}/H$(means)	$l/d_{\text{vis}}H$ (means)	$\bar{\gamma}/H$ (medians)	$l/d_{\text{vis}}H$ (medians)
8	1.48	1.49	1.43	1.43
10	1.98	1.57	1.30	1.45
12	1.69	1.55	1.57	1.48
14	1.49	1.57	1.44	1.63
8†	1.75	1.54	1.63	1.47

TABLE 3. Plume aspect ratios by wavenumber and by visual inspection, with averages using both means and medians shown. †Runs used a 16 cm width.

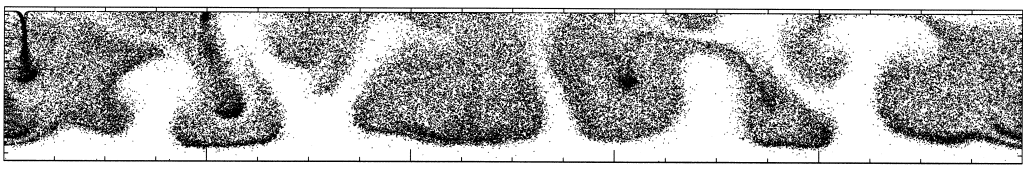

FIGURE 4. Example output of geotactic 'plumes' at pseudo-steady state.

.

We see that the plume spacing (measured by $\bar{\gamma}$) also increases with fluid height. Harashima *et al.* (1988) obtained similar qualitative results with their continuum model. They also report that their plumes had a constant aspect ratio. The l/d_{vis} information presented in table 3 indicate a plume aspect ratio of 1.4–1.6. Harashima *et al.* (1988) report a constant plume aspect ratio of 2.67. We have not yet performed controlled experiments to determine which differing parameter or feature of these models contributes to this observed difference in plume aspect ratio.

A qualitative feature of our geotaxis calculations is that the stability of the plumes increases as the fluid height decreases. This phenomenon is strikingly visible in experiments (as reported by Kessler 2000, private communication) and when one sees video simulations of the fluid–microbe system, and is also indicated quantitatively by the decrease in σ_d and σ_{cycle} as h decreases.

Tracks of ≈ 13 individual cells from a 14 mm height run are shown in figure 5(*a–d*). Note that some of the cells leave/enter the domain shown. The horizontal width in

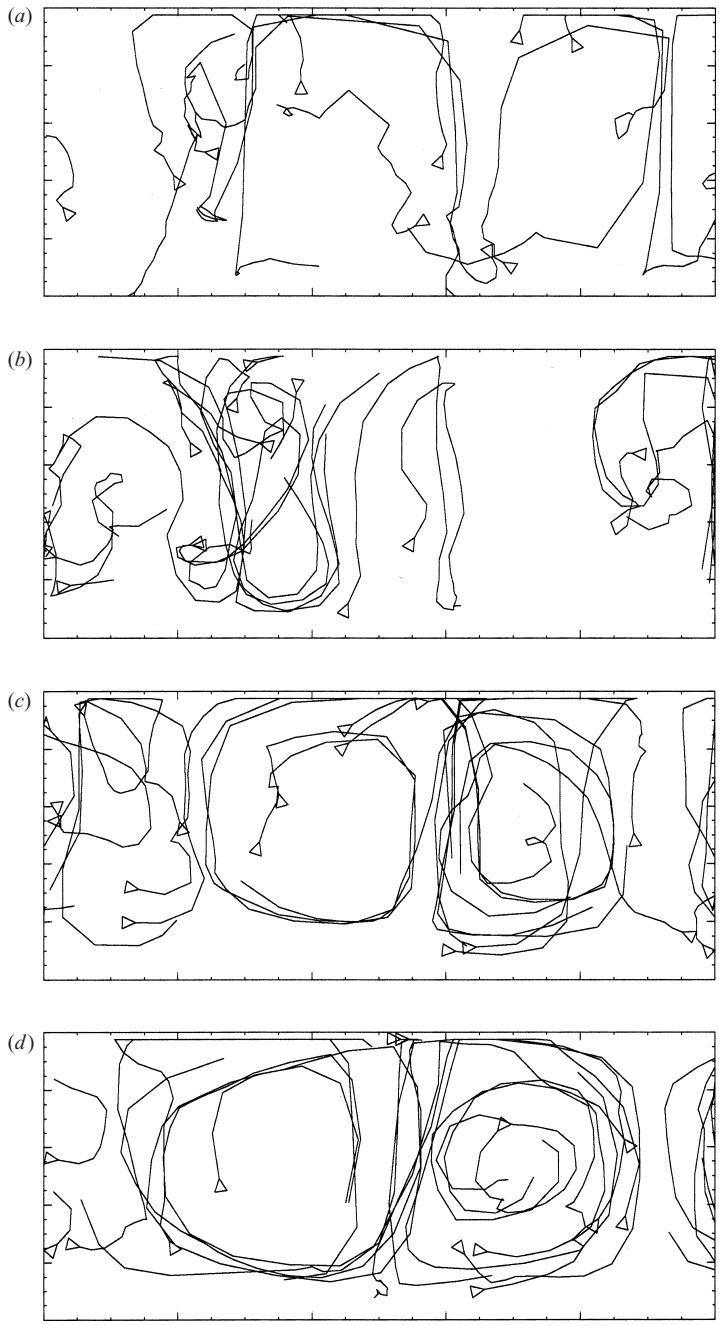

FIGURE 5. Trajectories of thirteen geotactic cells from a 14 mm height run over 200 s intervals. Triangles indicate starting locations. This figure should be compared to the gyrotactic cell trajectories depicted in figure 11. (*a*) 0–200 s, (*b*) 200–400 s, (*c*) 400–600 s, (*d*) 600–800 s.

these frames is 3.2 cm. The plumes are initially poorly defined, but later one can see the cell trajectories cycling through the plume. A plot of the height of a typical geotactic cell versus time is shown in figure 6. We see from the data in table 2 that the average time for a cell to cycle through a plume (t_{cycle}) increases with fluid domain height.

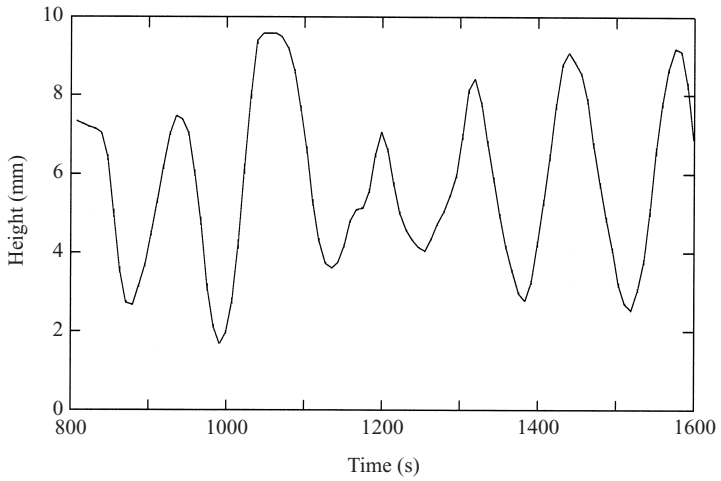

FIGURE 6. The height of a typical microbe versus time from a 10 mm geotactic run.

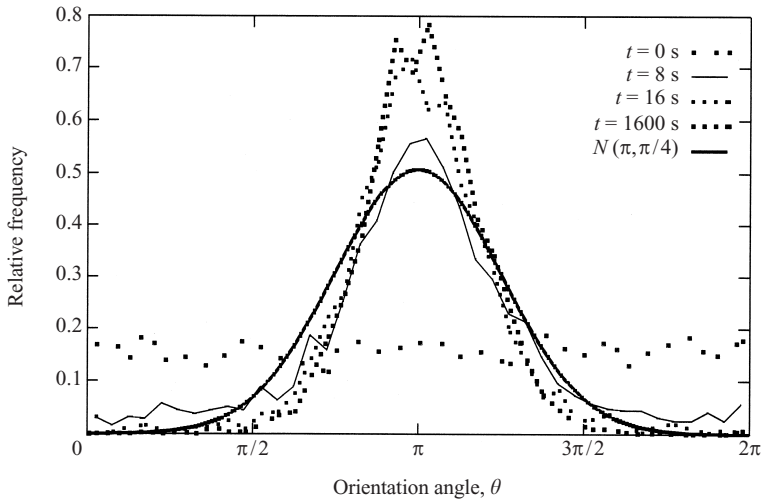

FIGURE 7. Distribution of orientation angles from a 10 mm geotactic run.

The variability in cycle times from cell to cell is measured by σ_{cycle}. The standard deviations of the cycle times vary from 15% to 41% of the cycle time means, while most are near 33%. This indicates a fairly good level of consistency over the cell population. This type of information might be useful in determining, for example, the time between maximal nutrient exposure for bioconvective cells (assuming the nutrient is at the surface).

We also plot the distribution of cell orientations in figure 7. Again, we use information from 2000 sample cells. We see that it takes a relatively short time (≈ 16 s) to reach the 'stable' Gaussian-like distribution for orientation angles. The distribution is not exactly Gaussian because of the constant geotactic reorientation towards $\theta = \pi$. The $N(\pi, \pi/4)$ distribution is plotted for comparison. Similar plots of the orientation angles of a collection of *Chlamydomonas nivalis* in a vertical plane are shown in Hill & Häder (1997).

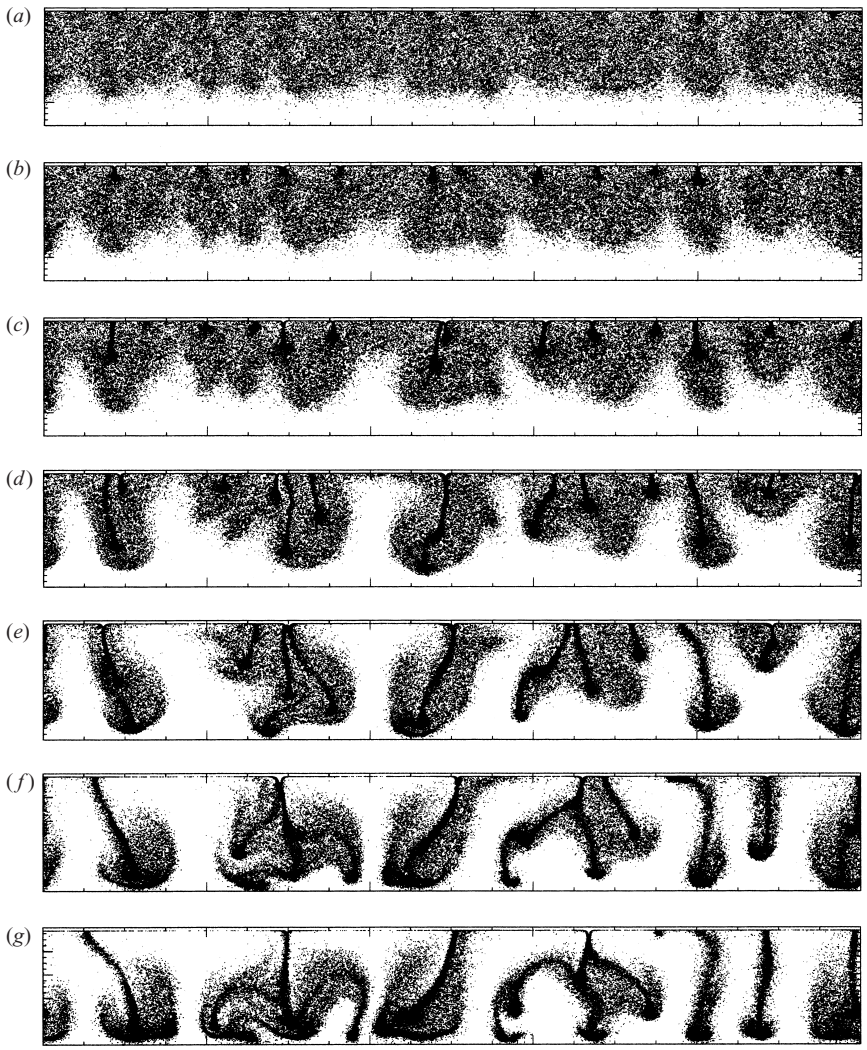

FIGURE 8. A sequence of snapshots capturing the initial overturning from a 12 mm gyrotactic run. Note that all of the approximately 85 700 particles representing the discrete microbes are depicted. Snapshots taken at times (*a*) 72 s, (*b*) 80 s, (*c*) 88 s, (*d*) 96 s, (*e*) 104 s, (*f*) 112 s, (*g*) 120 s.

4.2. *Gyrotaxis*

To determine the effects of combining the geotactic torque and the gyrotactic torque, we performed a series of runs with $\alpha_{\text{geo}} = 1$, $\alpha_{\text{vort}} = 9.52$, $\alpha_{\text{damp}} = 3.09$, and $\alpha_{\text{chemo}} = 0$. All other parameters are identical to those used in the geotactic runs presented above.

As expected, the initial overturning instability is similar to that in the geotaxis simulations (see figure 8*a–g*), but the long-term behaviour of gyrotactic plumes was very different. Qualitatively, the plumes formed and disappeared in distinct ways. When gyrotactic cells fall to the bottom in a plume, they have more of a tendency to stay near the bottom of the plume than the purely geotactic cells. This circumstance occurs because when the cells try to swim upwards, the vorticity-induced torque rotates them back into the plume. This densely packed collection of cells continues to drive the plume from the bottom. These bottom-standing plumes are discussed

	H	avg.$\bar{\gamma}$	avg.$\bar{d}$	avg.σ_d	avg.d_{vis}	avg.t_{cycle}	avg.σ_{cycle}
(*a*)	8	0.552	15.59	4.06	–	408.0	210.9
	10	0.568	15.67	4.73	–	428.5	214.5
	12	0.599	14.74	4.54	–	457.5	217.0
	14	0.627	14.38	4.87	–	489.0	223.4
	8†	1.041	7.814	0.62	7.3	147.00	43.8
(*b*)	8	0.537	15.67	4.44	–	412.5	210.3
	10	0.591	15.21	4.93	–	435.4	215.0
	12	0.601	14.64	4.49	–	458.0	216.1
	14	0.623	14.47	4.79	–	481.4	220.5
	8†	1.000	8.0	0.26	7.0	146.7	42.12

TABLE 4. Average values (*a*) by *mean* and (*b*) by *median* of computed wavelength $\bar{\gamma}$, wavenumbers $\bar{d}$, standard deviation of wavenumbers σ_d, visual number of plumes d_{vis}, the cycle time of a particle through a plume t_{cycle}, and the standard deviation of this cycle time σ_{cycle}. These are shown for each height h. †Runs used $\alpha_{\text{vort}} = 0.952$.

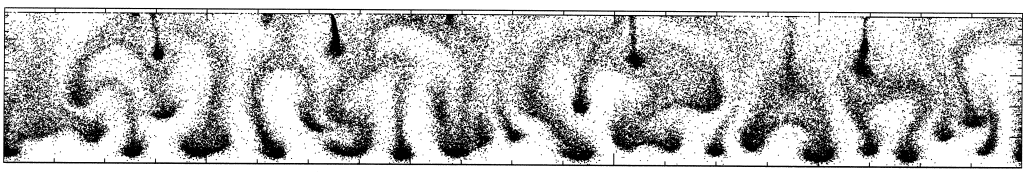

FIGURE 9. Example output of gyrotactic 'plumes' at pseudo-steady state.

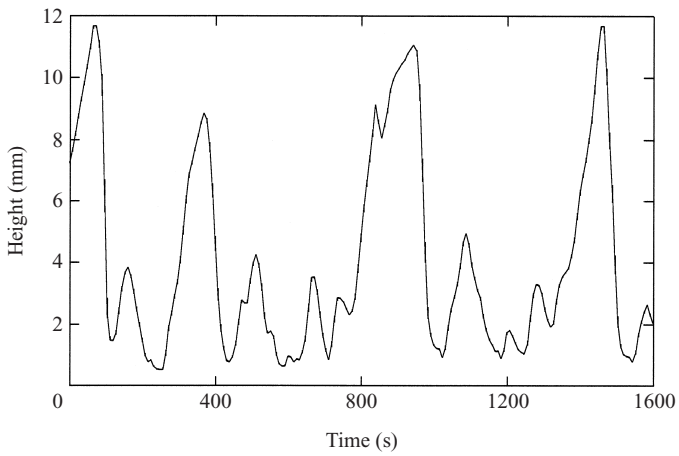

FIGURE 10. The height of a typical microbe versus time from a 12 mm height gyrotactic run. Note that the cell spends a considerable amount of time at the lower heights.

in Pedley & Kessler (1992) and also in the computational studies in Ghorai & Hill (2000).

We noted a qualitative change in the patterns formed when comparing the geotactic runs to the gyrotactic ones (compare figure 9 to figure 4). Whereas the geotactic plumes could often be quite stable, the gyrotactic plumes were much less so. In fact, it was often difficult to identify plumes at all because the gyrotactic patterns were much

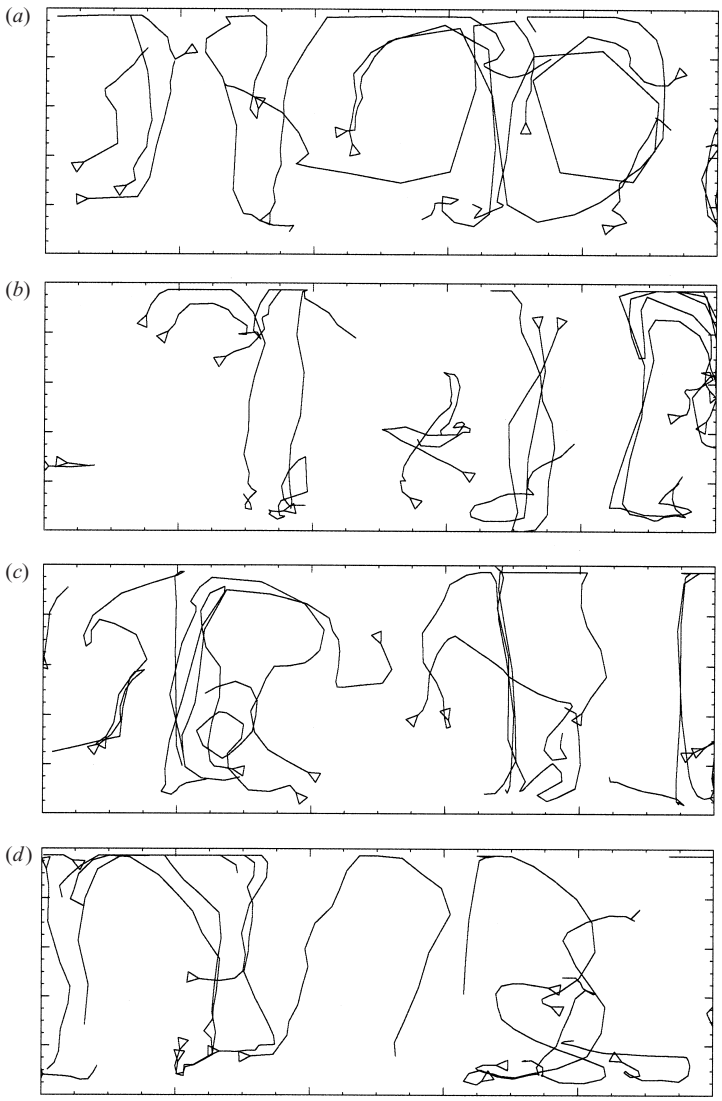

FIGURE 11. Trajectories of thirteen gyrotactic cells from a 12 mm height gyrotactic run over 200 s intervals. Triangles indicate starting locations. Compare to the geotactic cell tracks in figure 5. (*a*) 0–200 s, (*b*) 200–400 s, (*c*) 400–600 s, (*d*) 600–800 s.

more transient. Examining a single output was unilluminating (see figure 9), so d_{vis} was ignored for most of the runs.

As in the geotactic simulations, we performed five runs at each height, and the average results are presented in tables 4(*a*) and 4(*b*). The data indicate that the number of 'plumes' is much greater than in the geotactic case. This is supported by comparing the $\bar{d}$ values of the geotactic and gyrotactic runs. However, the plumes are not at all stable. In fact, in the gyrotactic runs σ_d is much larger than that computed in the geotactic runs discussed above.

Bees & Hill (1997) present data from experiments that examine bioconvective patterns of *Chlamydomonas nivalis* in a shallow dish as functions of suspension concentration, depth and time. Our computational results agree with the experimental

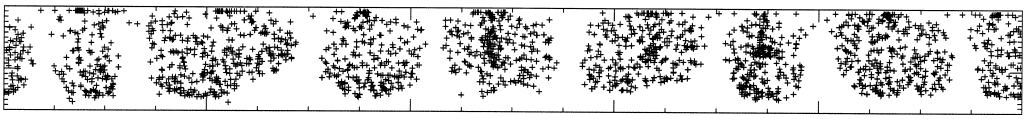

FIGURE 12. Stable plume formations from a shallow 8 mm height run with weak gyrotaxis at end of computation. While only 2000 particles representing the discrete microbes are shown, this calculation was performed with over 57 000 particles.

observation that plume wavelengths increase with suspension depth. More specifically, the experiments in Bees & Hill (1997) that most closely correspond to our computational experiments are (i) where the cell concentration was 8.08×10^5 cells cm^{-3} at a suspension depth of 5.22 mm, and (ii) where the cell concentration was 1.02×10^6 cells cm^{-3} at a suspension depth of 7.29 mm. The experimentally observed plume wavelength early on in the experiments was (i) 4.81 mm and (ii) 6.93 mm. In a container that was 8 cm wide (as in the computations), this would correspond to ≈ 11.5 and 16.6 plumes, respectively. Note that our computations for $\bar{d}$ in the 8 mm gyrotactic runs predict ≈ 15.6 plumes, and are thus consistent with these experiments. In fact, our geotaxis calculations only predicted ≈ 7 plumes.

The t_{cycle} values computed for the gyrotactic runs are large compared to the sampled computation time of 800 s (indicating small wavenumbers), and their relatively high standard deviations (σ_{cycle}) indicate that they are not a good measure of the time it takes for a gyrotactic cell to loop through a plume. This is due to the fact that cells in gyrotactic plumes tend to stay at the bottom of the plume for a longer period of time than purely geotactic cells. A plot of the height of a typical gyrotactic cell versus time is shown in figure 10. To present another perspective of individual gyrotactic cells, figure 11(*a–d*) shows ≈ 11 gyrotactic cell tracks. These should be compared to the geotactic cell tracks in figure 5(*a–d*). Note that the geotactic tracks span more width and are more regular than the gyrotactic tracks. In the geotactic tracks, one can observe the cycling through the plume. The gyrotactic tracks, on the other hand, indicate narrower, irregular plumes that have a denser core at their bottom.

To determine the effect of the gyrotactic weighting parameter α_{vort} we performed a series of runs with $\alpha_{\mathrm{vort}} = 0.952$. As expected, patterns closer to those of purely geotactic cells are achieved. In addition, the plumes seem to be more stable. The data for these runs (see table 4) indicate not only very stable plumes, but $\bar{d}$ indicates one more plume than in the purely geotactic runs. Visual inspection (d_{vis}) confirms this (see figure 12). Again, only 2000 cells are shown in this figure.

5. Numerical results: chemotaxis

In this section we present simulations of the coupled fluid–micro-organism–chemical system using both a gradient-detecting chemotaxis model and a run-and-tumble model.

We consider the rectangular, horizontally periodic domain $\Omega_R = [0, l] \times [0, H]$ with width $l = 2$ cm and height $H = 5$ mm. The numerical mesh was taken to be $N_x = 62$, $N_y = 26$. The boundary conditions for the fluid velocity at the upper surface $y = H$ are $u_y = 0$ and $v = 0$. At the bottom of the rectangle $y = 0$, the fluid velocity is zero. The number of computational cells was $N_m = 80\,000$, giving a three-dimensional cell concentration of $\approx 2.26 \times 10^7$ cells cm^{-3}. Initially, the cells are uniformly distributed in the rectangle. The cell parameters are given in table 5. Random components were chosen to be $\mu_\theta = 0$ rad, $\sigma_\theta = \pi/4$ rad s^{-1}, $\mu_s = 0\,\mu\mathrm{m\,s}^{-1}$, and $\sigma_s = 0.1 s_0\,\mathrm{s}^{-1}$.

Description	Symbol	Value
Cell density	ρ_m	$1.10\,\mathrm{g\,cm^{-3}}$
Cell volume	v_m	$1.8 \times 10^{-13}\,\mathrm{cm^3}$
Base cell swimming speed	s_0	$30\,\mu\mathrm{m\,s^{-1}}$

TABLE 5. Physical cell characteristics used to represent a 'typical' bacterium.

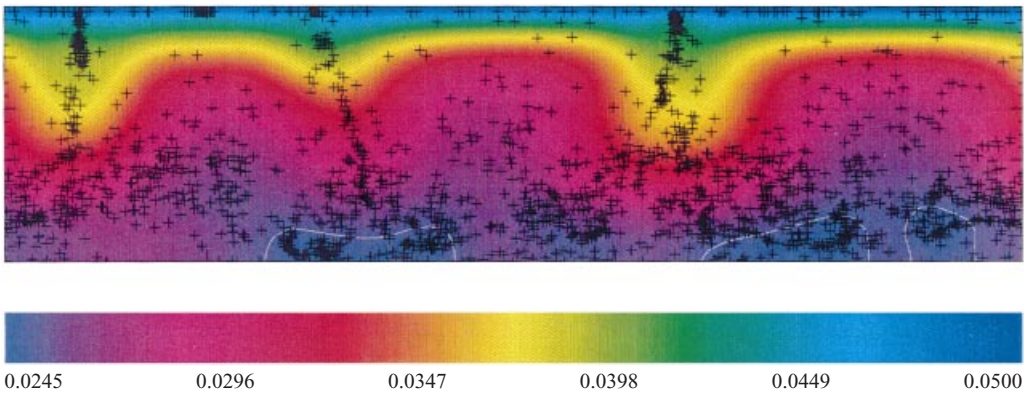

FIGURE 13. A snapshot of the microbe positions and chemical concentrations shortly after the initial plumes have started falling (at $t = 320\,\mathrm{s}$). A region of depleted chemical where $c < c_{\mathrm{min,mot}}$ (below the white line) has just appeared. While only 2000 particles representing the discrete microbes are shown, this calculation was performed with 80 000 particles.

In these chemotaxis simulations, we are also tracking the advection, diffusion, and uptake of a chemical in (2.3). The non-dimensional chemical concentration at the upper surface is fixed at $c_0 = 0.05$, and $\partial c/\partial y = 0$ at the bottom of the rectangle. Initially, the concentration is uniform $c = c_0$. We used a chemical diffusion coefficient $D = 1 \times 10^{-4}\,\mathrm{cm^2\,s^{-1}}$, which is much larger than that of oxygen ($2 \times 10^{-5}\,\mathrm{cm^2\,s^{-1}}$). This non-physical diffusion coefficient was chosen to accelerate the onset of plume formation and other qualitative features of this model.

Note that in the simulations presented below, we did not include torques due to gyrotaxis, in order to isolate the effects of chemotaxis. Of course, gyrotactic torques need to be included in a comprehensive model of chemotactic microbes.

5.1. *Gradient-detecting chemotaxis results*

We first consider microbes that can directly detect spatial gradients in c, and can identify a preferred orientation pointing in the direction of maximal increase of chemical. The torque balance equation (3.5) reduces to

$$\frac{\mathrm{d}\theta_k}{\mathrm{d}t} = -\frac{\alpha_{\mathrm{chemo}}}{\beta\alpha_{\mathrm{damp}}}(\theta_k - \theta_g)H(|\nabla c| - \epsilon). \tag{5.1}$$

Note that the ratio $\alpha_{\mathrm{chemo}}/\beta\alpha_{\mathrm{damp}}$ determines the time scale of reorientation. In particular, we set this ratio so that, in a steady concentration field, a microbe would be oriented to within 1% of its preferred orientation in 20 s.

The swimming speed of these 'intelligent' microbes depends upon the chemical concentration at their locations. In these simulations, we assume that when this concentration falls below a threshold $c_{\mathrm{min,mot}}$, the cells do not swim. The function $f(c)$

FIGURE 14. Pseudo-steady-state cell and chemical concentrations for gradient-detecting chemotaxis at $t = 1600$ s. The white line represents the $c = c_{\min,\mathrm{mot}}$ threshold, below which the cells are not swimming. Although the cells are non-motile in this region, they are still advected by the fluid.

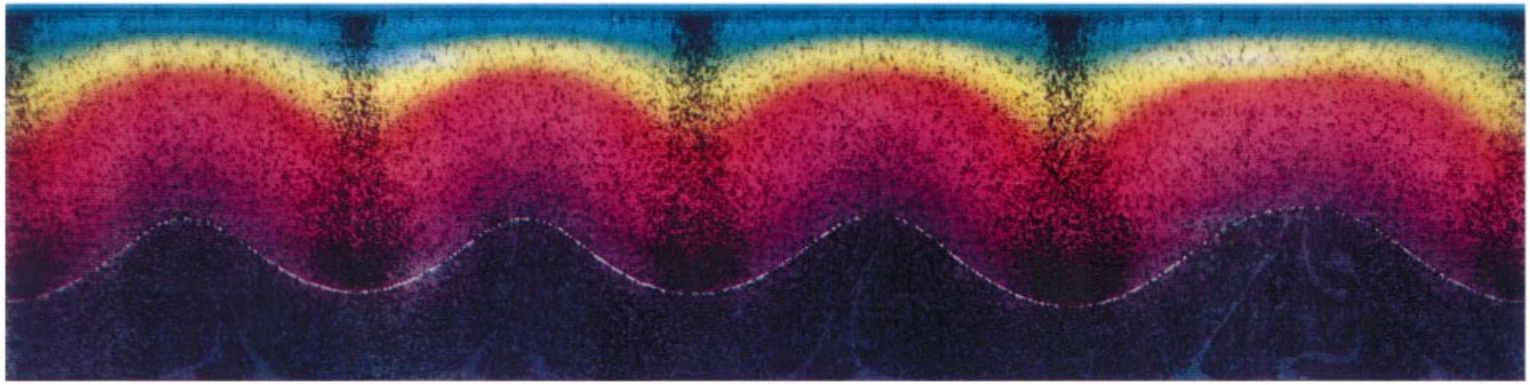

FIGURE 16. Pseudo steady-state cell and chemical concentrations for run-and-tumble chemotaxis at $t = 1600$ s. The white line represents the $c = c_{\min,\mathrm{mot}}$ threshold, below which the cells are not swimming. Although the cells are non-motile in this region, they are still advected by the fluid.

in (3.8) is, therefore,

$$f(c) = \begin{cases} 0 & \text{if } c < c_{\text{min,mot}} \\ s_0 & \text{if } c \geqslant c_{\text{min,mot}}. \end{cases} \tag{5.2}$$

We choose the chemical consumption function $R(c)$ in (2.3) to be

$$R(c) = -R_0 c g(c), \tag{5.3}$$

where

$$g(c) = \begin{cases} 0 & \text{if } c < c_{\text{min,con}} \\ \dfrac{e}{e-1}\left(1 - e^{-\left(\frac{c-c_{\text{min,con}}}{c_0-c_{\text{min,con}}}\right)^{0.4}}\right) & \text{if } c \geqslant c_{\text{min,con}}. \end{cases} \tag{5.4}$$

A similar form of saturation function was used in Hillesdon *et al.* (1995) for their analytic chemotactic model.

In the following simulations, we set the concentration threshold for consumption to be $c_{\text{min,con}} = 0.0245$, and the concentration threshold for motility to be $c_{\text{min,mot}} = 0.025$. Because $c_{\text{min,con}} < c_{\text{min,mot}}$ we will have a region where the cells are no longer motile, but are still consuming the chemical. We used a gradient detection cutoff of $\epsilon = 0.01$ (see equation (2.9)), below which a cell cannot detect a preferred orientation. Note that $|\nabla c|$ is generally very low ($< \epsilon$) in the region where $c < c_{\text{min,mot}}$.

Initially, $|\nabla c| < \epsilon$ everywhere, and none of the cells has a preferred orientation. As the cells consume the chemical, $|\nabla c|$ increases near the surface because of the chemical source there. At some point, this gradient exceeds the threshold of ϵ, and the cells in those regions detect a preferred orientation pointing towards the surface. They begin directed upswimming. This region, where $|\nabla c| \geqslant \epsilon$, grows downwards from the surface, eventually causing all of the cells to undergo directed upswimming. At this stage, $c \geqslant c_{\text{min,mot}}$ everywhere. (This initial cell progression agrees with the analytic model in Hillesdon *et al.* 1995.) Eventually, enough cells reach the surface, and an overturning instability begins. The concentration does not fall below $c_{\text{min,mot}}$ until plumes first reach the bottom (see figure 13).

Once the initial instability is over, a region containing non-motile cells emerges (where $c < c_{\text{min,mot}}$) from the bottom of the domain. The cells outside this region continue to swim up chemical gradients. Note that this swimming is not uniformly upwards: once a plume forms, it entrains chemical from the surface and transports it downwards, causing concentration gradients with horizontal components. In addition, the cells create concentration gradients themselves due to their consumption of chemical. The cells are also advected by the fluid flow, not necessarily in the direction of the gradient.

A pattern emerges: nearby cells swim laterally into the plumes, reinforcing them, often from the bottom of the plume. The chemical reaches a pseudo-steady state where the consumption of chemical in the $c_{\text{min,con}} < c < c_{\text{min,mot}}$ region balances with the diffusion/advection of chemical from the surface. The line where $c = c_{\text{min,mot}}$ threshold remains relatively stable while the cells continue to drive the plume (see figure 14). This qualitative feature of bottom-driven plumes is very similar to what was observed in gyrotactic plume dynamics in the previous section.

Cells at the bottom of the domain often spent time in the $c < c_{\text{min,mot}}$ region. They may be revived in one of two ways. One way is for a nearby plume to move slightly, thus moving the region where the entrained chemical has a concentration $c \geqslant c_{\text{min,mot}}$. If the downwelling velocity of the plume increases, the region in which $c \geqslant c_{\text{min,mot}}$ increases slightly, reviving the cells underneath the plume. The second way for a

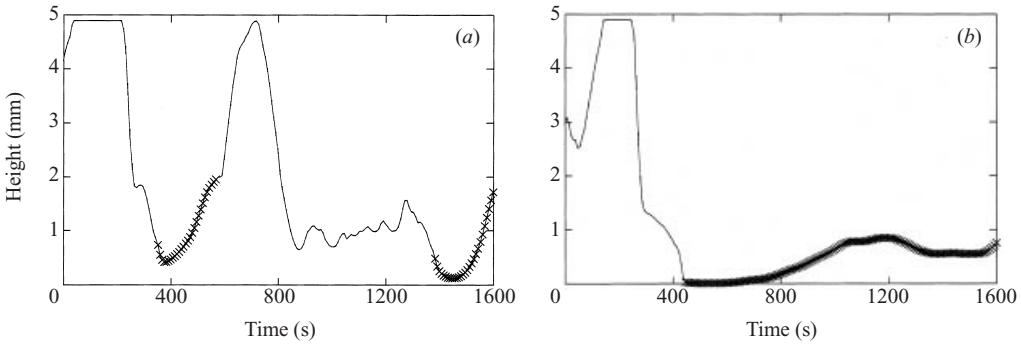

FIGURE 15. Height of a gradient-detecting chemotactic cell versus time. The × indicate that the chemical concentration at the cell site is less than that required for motility ($c < c_{\min,\mathrm{mot}}$). (*a*) This cell has moved into and out of the non-motile region. (*b*) This cell seems to be stuck in the non-motile region.

cell to be revived is for the fluid flow to scoop up the cells near the surface of the $c < c_{\min,\mathrm{mot}}$ region, and advect them into the $c \geqslant c_{\min,\mathrm{mot}}$ region. This *shearing* effect is ongoing and appears (visually) to account for most revived cells. Non-motile cells are more likely to be carried into $c \geqslant c_{\min,\mathrm{mot}}$ regions by the fluid flow than to have $c \geqslant c_{\min,\mathrm{mot}}$ concentrations transported to them.

The height of a typical active cell is shown in figure 15(*a*). This cell was advected into the $c \geqslant c_{\min,\mathrm{mot}}$ regime by the fluid flow at ≈ 600 s, and appears to be leaving the $c < c_{\min,\mathrm{mot}}$ region at the end of the run. The small oscillations between times 800 and 1400 indicate the cell was near the bottom of a plume, constantly swimming back into it whenever it was ejected from the bottom. The cells collect at the bottom of the plume and drive it much like the gyrotactic cells. Figure 15(*b*) shows the height of a cell that became 'trapped' under the $c = c_{\min,\mathrm{mot}}$ threshold.

5.2. *Run-and-tumble chemotaxis results*

It is generally believed that bacteria cannot directly sense a spatial gradient in chemical concentration, but respond to temporal changes in the concentration they experience by reorienting less frequently if this concentration is increasing. This causes the chemotactic microbes to move, on average, into regions of higher chemical concentrations. Since we have a discrete representation of cells, we are able to track the chemical concentration at the cell sites as a function of time. We implemented the run-and-tumble chemotaxis model presented in Dillon *et al.* (1995), that calculates the probability of a reorientation as a function of the cell's recent chemical history.

More specifically, we assume that the durations of the run intervals τ for a microbe are exponentially distributed with probability density function

$$g(\tau) = \lambda_k \exp(-\lambda_k \tau), \tag{5.5}$$

which has mean and standard deviation $1/\lambda_k$.

Chemotactic cells tumble less frequently if the cell experiences an increase in chemical concentration over a period of time. We assume that the parameter λ_k, which determines the tumbling probability, is a function of the chemical concentration at the cell site over the cell's recent history. We choose

$$\lambda_k(t) = \begin{cases} \Lambda_0 & \text{if } c(x_k(t),t) - c(x_k(t-\Delta t), t-\Delta t) < 0 \\ \Lambda_1 & \text{if } c(x_k(t),t) - c(x_k(t-\Delta t), t-\Delta t) \geqslant 0, \end{cases} \tag{5.6}$$

where Λ_0, Λ_1, and Δt are positive constants. Note that Δt is not the timestep of the numerical method, but a longer time interval during which the history is retained ($\Delta t = 1$ s for the case presented below).

The outline of this procedure for updating the orientation angle of an individual microbe is:

(*a*) compute the value of λ_k for each microbe;

(*b*) for each k, choose $y \in [0, 1]$ from a uniform distribution. If $y \leqslant 1 - \exp(-\lambda_k \Delta t)$ then do step (*c*). This determines whether a cell actually tumbles;

(*c*) choose the tumble angle and set θ_k.

For further details, we refer the reader to Dillion *et al.* (1995).

We set the characteristic run time between tumbles to be $t = 1$ s if the concentration of chemical at the cell is decreasing ($\Lambda_0 = 1$) and $t = 10$ s if this concentration is increasing ($\Lambda_1 = 0.1$). In addition, we assume that cell reorientations occur instantaneously.

Compared to the gradient-detecting case presented above, plumes formed more slowly with this run-and-tumble chemotaxis mechanism. Although the cells have the same swimming speed as in the gradient-detecting case, they are not spatially directed, and thus do not have as strong a bias towards swimming up concentration gradients. This causes more of the cells to remain in the lower regions of the domain, both delaying initial plume formation due to a lack of sufficient cell mass at the surface, and causing $c_{\min,\mathrm{mot}}$ to be attained sooner. Overall, the plumes are more loosely defined than in the gradient-detecting case (compare figure 16 to figure 14).

6. Summary

We have presented a robust and versatile computational model of bioconvection, where a collection of geotactic, gyrotactic or chemotactic micro-organisms interact with a viscous, incompressible fluid. Plume formation and stability has been studied for purely geotactic as well as gyrotactic microbes in rectangular chambers of varying depth. As in the recent calculations of Ghorai & Hill (2000), we demonstrate that bottom-standing gyrotactic plumes are regeneratively reinforced in the vicinity of the bottom of the chamber, plume wavelengths increase slightly with depth, and plume stability decreases with depth.

We believe that the discrete representation of the microbes facilitates the direct evaluation of cell orientation in response to environmental cues and stochastic effects. Moreover, the work required for evaluating the interaction of N microbes is only $O(N)$, and not $O(N^2)$. This is because their interaction is mediated through the fluid velocity field. Hence, while a full three-dimensional model will require many more discrete particles, we expect the computational work to be feasible.

The actual dynamical system consisting of fluid and suspended swimming organisms is obviously three-dimensional, as are the basic modelling equations. While the computations presented in this paper are two-dimensional, they provide results that match the spatial patterns and long-time temporal dynamics of actual experiments remarkably well. We demonstrate that this modelling framework can be used to test hypotheses concerning the coupled effects of microbial behaviour, fluid dynamics and molecular mixing. We have not attempted as yet to tailor our model to specific organisms or nutrients. Nevertheless, these detailed computational studies will be the subject of future work, as will be a full three-dimensional implementation.

Sandia is a multiprogram laboratory operated by Sandia Corporation, a Lockheed Martin Company, for the United States Department of Energy under Contract DE-AC04-94AL85000. The work of Lisa Fauci was supported by the National Science Foundation grant DMS-9805492 and DMS-9709754.

REFERENCES

Bees, M. A. & Hill, N. A. 1997 Wavelengths of bioconvection patterns. *J. Expl Biol.* **200**, 1515–1526.

Berg, H. C. 1983 *Random Walks in Biology*. Princeton University Press.

Childress, S. & Peyret, R. 1976 A numerical study of two-dimensional convection by motile particles. *J. Méc.* **15** (5), 753–779.

Dillon, R., Fauci, L. & Gaver, D. 1995 A microscale model of bacterial swimming, chemotaxis and substrate transport. *J. Theor. Biol.* **177**, 325–340.

van Doormaal, J. P. & Raithby, G. D. 1984 Enhancements of the SIMPLE method for predicting incompressible fluid flows. *Numer. Heat Transfer* **7**, 147–163.

Ghorai, S. & Hill, N. A. 1999 Development and stability of gyrotactic plumes in bioconvection. *J. Fluid Mech.* **400**, 1–31.

Ghorai, S. & Hill, N. A. 2000*a* Periodic arrays of gyrotactic plumes in bioconvection. *Phys. Fluids.* **12**, 5–22.

Ghorai, S. & Hill, N. A. 2000*b* Wavelengths of gyrotactic plumes in bioconvection. *Bull. Math. Biol.* **62**, 429–450.

Happel, J. & Brenner, H. 1987 *Low Reynolds Number Hydrodynamics*. Prentice Hall.

Harashima, A., Watanabe, M. & Fujishiro, I. 1988 Evolution of bioconvection patterns in a culture of motile flagellates. *Phys. Fluids* **31**, 764–775.

Hill, N. A. 1997 *Case Studies in Mathematical Modeling – Ecology, Physiology, and Cell Biology*, chap. 15: Bioconvection, pp. 339–351. Prentice Hall.

Hill, N. A. & Häder, D. P. 1997 A biased random walk model for the trajectories of swimming micro-organisms. *J. Theor. Biol.* **186**, 503–526.

Hill, N. A., Pedley, T. J. & Kessler, J. O. 1989 Growth of bioconvection patters in a suspension of gyrotactic micro-organisms in a layer of finite depth. *J. Fluid Mech.* **208**, 509–543.

Hillesdon, A. J., Pedley, T. J. & Kessler, J. O. 1995 The development of concentration gradients in a suspension of chemotactic bacteria. *Bull. Math. Biol.* **57**, 299–344.

Jones, M. S., LeBaron, L. & Pedley, T. J. 1994 Biflagellate gyrotaxis in a shear flow. *J. Fluid Mech.* **281**, 137–158.

Kessler, J. O. 1986*a* Individual and collective fluid dynamics of swimming cells. *J. Fluid Mech.* **173**, 191–205.

Kessler, J. O. 1986*b* The external dynamics of swimming micro-organisms. In *Progress in Phycological Research* (ed. F. E. Round & D. J. Chapman), vol. 4, pp. 257–307. Bristol: Biopress.

Kessler, J. O. 1989 Path and pattern – the mutual dynamics of swimming cells and their environment. *Comments Theoretical Biology* **1** (2), 85–108.

Kessler, J. O., Strittmatter, R. P., Swartz, D. L. and others 1995 Paths and patterns: The biology and physics of swimming bacterial populations. In *Biological Fluid Dynamics* (ed. C. P. Ellington and T. J. Pedley), vol. 49, Symp. Soc. Expl Biol, pp. 91–107.

Kessler, J. O., Burnett., G. D. and Remick, K. E. 2000 Mutual dynamics of swimming micro-organisms and their fluid habitat. In *Nonlinear Science at the Dawn of the 21st Century* (ed. Christiansen, P. L. and Soerensen, M. P. and A. C. Scott), vol. 542, Springer Lecture Notes in Physics, pp. 409–426. Heidelberg.

Levandowsky, M., Childress, W. S., Spiegel, E. A. & Hunter, S. H. 1975 A mathematical model of pattern formation by swimming microorganisms. *J. Protozool.* **22** (2), 296–306.

Metcalfe, A. M. & Pedley, T. J. 1998 Bacterial bioconvection: weakly nonlinear theory for pattern selection. *J. Fluid Mech.* **370**, 249–270.

Patankar, S. V. 1980 *Numerical Heat Transfer and Fluid Flow*. Washington, D.C.: Hemisphere.

Pedley, T. J., Hill, N. A. & Kessler, J. O. 1988 The growth of bioconvection patterns in a uniform suspension of gyrotactic micro-organisms. *J. Fluid Mech.* **195**, 223–237.

Pedley, T. J. & Kessler, J. O. 1987 The orientation of spheroidal micro-organisms swimming in a flow field. *Proc. R. Soc. Lond.* B **231**, 47–70.

Pedley, T. J. & Kessler, J. O. 1990 A new continuum model for suspensions of gyrotactic micro-organisms. *J. Fluid Mech.* **212**, 155–182.

Pedley, T. J. & Kessler, J. O. 1992 Hydrodynamic phenomena in suspensions of swimming micro-organisms. *Annu. Rev. Fluid Mech.* **24**, 313–358.

Plesset, M. S. & Winet, H. 1974 Bioconvection patterns in swimming micro-organism cultures as an example of Rayleigh Taylor Instability. *Nature*. **248**, 441–443.

Ramia, M., Tullock, D. L. & Phan-Thien, N. 1993 The role of hydrodynamic interaction in the locomotion of microorganisms. *Biophys. J.* **65**, 755–778.